RSC Advances

ROYAL SOCIETY OF CHEMISTRY

www.rsc.org/advances

Graphical content entry:

Porous ZnO and ZnO-NiO nanostructures were found to catalyze decomposition of ammonium perchlorate, and ZnO to biosense DNA hybridization.

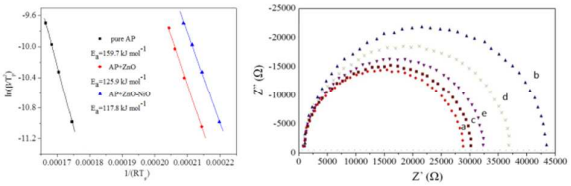

Porous ZnO and ZnO-NiO composite nano/microspheres: synthesis, catalytic and biosensor properties†

Ji-Min Yang,[ab] Wei Zhang,[b] Qing Liu[a] and Wei-Yin Sun*[a]

[a] *Coordination Chemistry Institute, State Key Laboratory of Coordination Chemistry, School of Chemistry and Chemical Engineering, Nanjing National Laboratory of Microstructures, Nanjing University, Nanjing 210093, China. E-mail: sunwy@nju.edu.cn; Fax: +86 25 83314502*

[b] *School of Chemistry & Chemical Engineering, Linyi University, Linyi 276005, China*

† Electronic supplementary information (ESI) available: Immobilization and hybridization of DNA, XRD, FT-IR, EDS, sorption isotherms for N_2, pore size distribution, DSC and TGA data. See DOI:

Porous ZnO and ZnO-NiO composite nano/microspheres have been successfully synthesized by calcination of non-doped and Ni(II)-doped precursors in air, respectively. The catalytic effect was investigated for porous ZnO and ZnO-NiO composite nano/microspheres on the thermal decomposition of ammonium perchlorate (AP). The ZnO-NiO composite nano/microspheres showed remarkable catalytic effect for the thermal decomposition of AP. The decomposition temperature was decreased by 144.5 °C and the apparent activation energy was significantly decreased to 117.8 kJ mol^{-1}, much lower than 159.7 kJ mol^{-1} for pure AP. The catalytic capacity of ZnO-NiO composite nanostructures is higher than that of most materials reported to now. As a result, porous ZnO-NiO composite nano/microstructures could be a promising candidate material for an AP-based propellant. In addition, using the as-prepared porous ZnO microspheres, we have successfully prepared a novel, ultrahigh resolution electrochemical impedance DNA biosensor for the enhanced detection of the

PML/RARA fusion gene in acute promyelocytic leukemia with detection limit of 2.2×10^{-13} mol L^{-1}, therefore, it can act as biosensing materials for recognition of DNA hybridization.

Introduction

In the past decade, the fabrication of metal-organic frameworks (MOFs) with various nanostructures have attracted considerable scientific interest from coordination chemists on account of their novel framework structures, topologies and interesting properties.[1–5] By thermal decomposition of MOFs nanostructures, the resulting nanoscale metal oxides, metal oxide/amorphous carbon, or metal/graphene have been obtained.[6–9] Due to the novel nanostructures, these materials display functional properties such as effective catalysis, gas storage capacities and antibacterial activities.[7,8,10]

Zinc oxide (ZnO), which is a n-type semiconductor with a wide band gap and a bio-safe and biocompatible material,[11-13] has attracted great research interests due to its unique properties and wide applications in transparent electronics, piezoelectric devices, chemical and biological sensing, and catalytic reactions.[14-19] To date, various methods have been used for preparation of nano/microscale ZnO with diverse shapes including nanorods,[20,21] nanowires,[22] nanobelts,[23] nanorings,[24] nanosheets,[25] nanospheres[26] and tetrapods.[27] Such ZnO nanostructures show interesting optoelectronic and catalytic properties. On the other hand, nickel oxide (NiO) is an important p-type semiconductor and has been considered as one of the promising materials in supercapacitors,[28,29] gas sensors,[30,31] catalysis[32] and chemical and biological sensors.[33,34]

The nano-sized composite materials have attracted much attention due to their enhanced electronic, magnetic, catalytic, optical, thermal properties as compared with the non-composite ones.[35] As typical examples, the gas sensing properties of the ZnO-NiO composite for H_2S gas detection have been greatly improved,[36] CaO-Fe_3O_4 composite

nanospheres show enhanced catalytic performance,[37] and CuO-Fe_2O_3 composite nanoparticles can accelerate the catalytic decomposition of ammonium perchlorate (AP).[38] The individual chemical and physical properties of NiO or ZnO nanomaterials have been extensively demonstrated, while there has been less study on the preparation of ZnO-NiO composite nanostructures as a catalyst for the thermal decomposition of AP.

To date, various techniques have been reported for the detection of DNA such as optical, acoustic, gravimetric, and electronic approaches.[39] However, there are limitations in these approaches, such as time-consuming, poor precision and expensiveness. Recently, metal oxide nanostructures based biosensors for DNA detection exhibit powerful capability to convert the hybridization event into an analytical signal and have received considerable attention due to their simplicity, portability, sensitivity, and selectivity.[40] Such DNA biosensors contain high specificity to target sequences in the presence of non-complementary strands and show potential for detection of diseases and genetic disorders, environmental and food safety monitoring.[16,40,41] Immobilization of DNA on a given matrix is a crucial step for fabricating an electrochemical DNA biosensor. Various matrices such as metal oxide nanomaterials, composite nanomaterials and noble metal nanoparticles have been used as the support for probe immobilization.[42-47] Recently, nanosized metal oxides and composite nanomaterials have been used in various biosensor developments owing to their high surface area, chemical inertness, thermal stability, non-toxicity and good biocompatibility.[16,42-47] For example, a novel electrochemical impedance DNA biosensor for acute promyelocyticleukemia was developed by immobilizing a PML/RARA related 18-mer oligonucleotides ssDNA sequence on FePt-CNTs-GCE or FePt-GO-GCE or carbon ionic liquid electrode modified with nanosized ZnO.[16,47] Wang et al. also reported a DNA biosensor based on ZnO nanowires, multiwalled carbon nanotubes (MWCNTs) and gold nanoparticles for detection of sequence-specific target DNA.[48] However, porous ZnO nano/microspheres as

biosensing platform for detection of DNA hybridization have rarely been reported to now.

In this work, we have successfully synthesized porous ZnO and ZnO-NiO composite nano/microspheres by calcination of the precursors in air. Compared with the sole ZnO nano/microcrystals, the ZnO-NiO composite nano/microstructures exhibit high catalytic activity for the decomposition of AP. In addition, we present the advantages of incorporating porous ZnO and carbon ionic liquid electrode (CILE) for sensitive detection of PML/RARA fusion gene in acute promyelocytic leukemia.

Experimental

Materials and chemicals

Zinc(II) nitrate hexahydrate [$Zn(NO_3)_2 \cdot 6H_2O$, 99%], nickel(II) nitrate hexahydrate [$Ni(NO_3)_2 \cdot 6H_2O$, 98%], ammonium perchlorate (AP, 98%), acetic acid (HAc, 99.5%) N,N-dimethylformamide (DMF, 99.5%) and ethanol (C_2H_5OH, 99.7%) were obtained from Nanjing Chemical Reagent Co. Ltd. 2-Aminoterephthalic acid (H_2N-BDC, 98%) was purchased from Tokyo Chemical Industry Co. Ltd. All chemicals are analytically pure and were used as received without further purification.

Synthesis of precursor

Zinc-based coordination polymer particles designated as Zn-CPPs was prepared by modified procedures reported previously.[49,50] $Zn(NO_3)_2 \cdot 6H_2O$ (18.2 mg, 0.06 mmol), H_2N-BDC (5.4 mg, 0.03 mmol) and 10 μL HAc were dissolved in 30 mL DMF at room temperature. The mixture was transferred into a 43 mL Teflon-lined autoclave, which was sealed and maintained at 120 °C for 4 h. The reaction vessel was then taken out from the oven and allowed to cool to room temperature. The products were separated via centrifugation at 10000 rpm for 5 minutes, then 4 mL of DMF was added to 7 mL centrifuge tube including about 10 mg of the isolated products, and then the products were washed by ultrosonication under

ultrasonic irradiation at a frequency of 40KHz and an ultrasonic power output of 300 W (KH-300DE, Kunshan Hechuang Ultrasonics, China) for 5 minutes and isolated by centrifugation as mentioned above. The DMF washing was repeated for three times. The products were dried in a vacuum at 60 °C for 4 h. The precursor of nickel-doped zinc-based coordination polymer particles designated as Ni(II)-doped Zn-CPPs was synthesized by the same procedure used for preparation of Zn-CPPs, except that $Zn(NO_3)_2 \cdot 6H_2O$ (9.1 mg, 0.03 mmol) and $Ni(NO_3)_2 \cdot 6H_2O$ (8.9 mg, 0.03 mmol) were used. The chemical composition of the prepared Ni(II)-doped Zn-CPPs nano/microcrystals was determined by ICP-OES (inductively coupled plasma optical emission spectrometer).

Synthesis of nanocrystals

The as-obtained precursors were calcined in air at 500 °C with a heating rate of 2 °C min^{-1} (DRZ-3D, Longkou Electric Cooker Factory, China) to produce ZnO and ZnO-NiO composite nano/microspheres, respectively. The as-obtained ZnO-NiO composite nanocrystals comprise about 25% Ni(II) and 75% Zn(II) (ICP-OES).

Immobilization and hybridization of DNA

CILE, ZnO/CILE, immobilization and hybridization of DNA probe were prepared by modified procedures reported previously (See ESI).[16,45]

Characterization

The products were characterized by powder X-ray diffraction (PXRD) on a Bruker D8 Advance X-ray diffractometer with Cu Kα radiation (λ = 1.5418 Å) at room temperature. Field emission scanning electron microscopy (SEM) images and energy dispersive spectrometry (EDS) of the products were obtained on a field emission scanning electron micro-analyser (Hitachi S-4800), employing an accelerating voltage of 5 or 20 kV. Transmission electron microscopy (TEM) images were obtained on a JEM-2100 high resolution transmission microscope, employing an accelerating voltage of 200 kV. Inductively

coupled plasma optical emission spectrometer (ICP-OES) was measured on Optima 5300DV. FT-IR spectra were recorded in the range of 400-4000 cm^{-1} on a Bruker Vector22 FT-IR spectrophotometer using KBr pellets. Nitrogen sorption experiments at 77 K were carried out on a Belsorp-max volumetric gas sorption instrument. Surface areas were determined by the BET equation. Ultrahigh purity N_2 was used in the adsorption study. Prior to measurement of nitrogen sorption, the samples were activated under vacuum at 100 °C for about 10 h.

Catalytic measurements

To test the catalytic effect of ZnO and ZnO-NiO composite nano/microcrystals on the thermal decomposition of AP, a mixture of AP and catalytic particles was ground carefully for 10 min and was detected by a differential scanning calorimeter (DSC) and thermogravimetric analysis (TGA) on a Mettler-Toledo thermal analyzer under the nitrogen atmosphere in the temperature range from 30 to 500 °C with the different heating rate of 5, 10, 15 and 20 °C min^{-1}, respectively. The mass percentage of catalytic particles to AP in the mixture is 2%.

Electrochemical measurements

Electrochemical impedance spectroscopy (EIS) measurements of 1.0 mmol L^{-1} $K_3Fe(CN)_6$ and 1.0 mmol L^{-1} $K_4Fe(CN)_6$ were performed on an electrochemical analyzer (EC500, Wuhan GaossUnion Company, China) with 0.1 mol L^{-1} KCl as the supporting electrolyte. A conventional three-electrode system was used with a modified CILE as working electrode, a saturated calomel electrode as reference electrode and a Pt wire as the counter electrode. The AC voltage frequencies ranged from 10 kHz to 0.1 Hz.

Results and discussion

The simple route for the fabrication of ZnO-NiO composite nanostructures is shown in Scheme 1. The MOF precursor was readily obtained by mixing $Zn(NO_3)_2 \cdot 6H_2O$, $Ni(NO_3)_2 \cdot 6H_2O$, H_2N-BDC and HAc in DMF. Fig. 1 shows typical field emission SEM

images of the precursors. Without addition of $Ni(NO_3)_2 \cdot 6H_2O$, the results shown in Figs. 1a and 1b indicate that Zn-CPPs is composed of uniform microspheres with diameter of about 600 nm. Further observation reveals that the Ni(II) doping results in significant change in the size of the precursor microspheres. The sizes of Ni(II)-doped particle microspheres are obviously smaller than that of the Zn-CPPs, which may be related to the effect of Ni(II) doping on the precursor structure. The average diameter of the Ni(II)-doped Zn-CPPs is around 300 nm (Figs. 1c and 1d). Fig. S1 (ESI†) shows the PXRD patterns of the precursors. Both of the as-obtained products are amorphous. The FT-IR spectral data and EDS analysis are shown in Figs. S2 and S3 (ESI†), respectively. The characteristic bands around 1581 and 1394 cm^{-1} are the stretching vibrations of $\nu_{as}(-COO^-)$ and $\nu_s(-COO^-)$ of the carboxylate in $H_2N\text{-}BDC^{2-}$, and the peaks of Ni, Zn, C, N and O are easily found in the EDS, indicating that the precursors might be amorphous coordination polymer nano/microstructures.

The ZnO and ZnO-NiO composite nano/microspheres were prepared by calcination of the corresponding precursor at 500 °C in air. The PXRD patterns of the calcinated products are presented in Fig. 2. In pure ZnO (Fig. 2a), all the peaks are in good accordance with the standard spectrum of ZnO (JCPDS 36-1451), which means that the precursor was completely transformed into the ZnO nano/microsphere. In ZnO-NiO composites (Fig. 2b), several weak additional diffraction peaks appeared, which corresponds to NiO (JCPDS 47-1049). From the PXRD patterns it is clear that the precursors have been completely converted to ZnO-NiO composites. Fig. 3 shows the morphology of the as-obtained products, it can be clearly seen that the original shape has been maintained after calcination at 500 °C for 1 h in air. The average diameter of ZnO and ZnO-NiO composite nano/microspheres are around 300 and 100 nm, respectively (Figs. 3a-3d). Fig. 4a shows a representative TEM image of the ZnO-NiO composite nanospheres. From high-magnification TEM images (Fig. 4b), it can be clearly seen that a large number of cracks and pores exist on the surface of the as-obtained products.

The high resolution TEM images are depicted in Figs. 4c and 4d. The interplanar distances of 0.210 nm and 0.247 nm are in good agreement with the (200) plane of cubic NiO and (101) plane of the hexagonal structure of ZnO, respectively. Fig. 5 shows the EDS mappings of ZnO-NiO composites. The SEM images correspond to the images of the EDS mapping of Ni(II) and Zn(II). The distributions of Ni(II) is consistent with that of Zn(II) in the mapping, suggesting that Ni(II) elements are well dispersed in the ZnO crystals. To investigate the porous structure of ZnO and ZnO-NiO composite nano/microspheres, nitrogen sorption measurements were performed. Nitrogen adsorption-desorption isotherms of the porous ZnO and ZnO-NiO composite nano/microstructures are shown in Fig. S4 (ESI†), and Fig. S5 (ESI†) exhibits the corresponding Barrett-Joyner-Halenda (BJH) pore size distribution plots, indicating that all of the products contain mesopores. The BET surface areas and pore volumes of the products are 17.62 $m^2 g^{-1}$ and 63.87 $mm^3 g^{-1}$ and 18.30 $m^2 g^{-1}$ and 190.01 $mm^3 g^{-1}$ for ZnO and ZnO-NiO nano/microspheres, respectively. The results are consistent with the observation of mesopores in the HRTEM image (Fig. 4d).

AP is the key component of composite solid propellants since its thermal decomposition characteristics directly influence the combustion behavior of the propellant. More specifically, the performance of solid propellants is closely associated with the reaction rate, activation energy and thermal decomposition temperature of AP. Generally speaking, the lower the pyrolysis temperature gets, the higher the combustion rate can be.[51,52] Some important factors like the type of the catalysts and the heating rate are crucial to the final decomposition temperature. Herein, we investigated the influence of catalytic activity of ZnO and ZnO-NiO composite nano/microspheres and the heating rate on the thermal decomposition of AP.

Fig. 6 shows the DSC curves of both pure AP and the mixtures of AP with the catalytic particles at a 2% mass basis with a heating rate of 10 °C min^{-1}. From Fig. 6a, it can be seen that the first endothermic peak at 240-250 °C is due to the crystal transformation of AP from

orthorhombic to cubic phase, the second exothermic peak at 310-340 °C is ascribed to the partial decomposition of AP, and the third exothermic peak around 420-440 °C corresponds to the thermal decomposition of AP.[7,19,52] When porous ZnO and ZnO-NiO composite particles were added to AP, all samples have similar endothermic peaks at around 242.8 °C, indicating that the particles have little effect on the crystallographic transition temperature of AP. However, in the relatively high temperature region, the samples containing catalytic particles have dramatic changes in the exothermic peaks of AP decomposition. When the as-obtained catalytic particles are added to AP, the original exothermic peak of pure AP at 432.3 °C disappeared and fused into one exothermic peak. The exothermic peak temperature was 302.2 and 287.8 °C for pure ZnO and ZnO-NiO composites, respectively. The exothermic temperature decreases by about 130.1 and 144.5 °C, respectively for the above two samples compared to the pure AP. The catalytic capacity of ZnO-NiO composite nanostructures is higher than that of most materials reported to now.[7,19,38,52] Furthermore, TGA curves of pure AP and mixture of AP with the catalytic particles are shown in Fig. 7. In the range from 30 to 500 °C, two weight loss steps are observed for pure AP (Fig. 7a), while for the mixture of AP with the catalytic particles (Figs. 7b and 7c) only one weight loss step is observed, in agreement with the DSC results.

To further study the catalytic effect of samples on the thermal decomposition kinetic parameters of AP, both pure AP and the mixtures of AP with ZnO or ZnO-NiO composite nano/microspheres were investigated by TGA and DSC with different heating rates from 5 to 20 °C min^{-1}, and the results are shown in Figs. S6 and S7 (ESI†). The decomposition temperature of AP with the samples containing catalytic particles is dependent on the heating rate and a slight increase of the exothermic temperature was accompanied with the increase of heating rate. Apparent activation energy (E_a) was calculated from the exothermic peak temperature dependence on the heating rate using the Kissinger correlation:

$$\ln\left(\frac{\beta}{T_P^2}\right) = \ln\left(\frac{AR}{E_a^2}\right) - \frac{E_a}{RT_p}$$

where, β is the heating rate in degree Celsius per minute, T_p is the peak temperature, R is the ideal gas constant, and A is the exponential factor. According to the above equation, the term $\ln(\beta/T_p^2)$ varies linearly with $1/(RT_p)$, yielding the kinetic parameters of apparent activation energy from the slope of the straight line.[18,53] The calculated results according to Kissinger method are shown in Fig. 8. For pure AP, apparent activation energy E_a is calculated to be 159.7 kJ mol^{-1}, which is close to the values reported previously.[18] In the presence of ZnO and ZnO-NiO composites, the apparent activation energies E_a of AP decomposition are decreased significantly to 125.9 and 117.8 kJ mol^{-1}, respectively. It can be seen that porous ZnO and ZnO-NiO composites exhibit good catalytic activity for AP decomposition. Moreover, the catalytic activity of ZnO-NiO composites is better than that of ZnO, in agreement with the activation energy E_a. It is well known that the electron transfer from ClO_4^- to NH_4^+ is the key in controlling the decomposition rate of AP.[52,54,55] As an excellent conductor, NiO has a smaller work function (4.3 eV) than the one of ZnO (5.2 eV),[55,56] electrons in ZnO-NiO composites can move faster than they do among ZnO, therefore, the ZnO-NiO composites offer more effective and accelerated electrons to speed up from ClO_4^- to NH_4^+ and lead to the lower exothermic temperature. On the other hand, it is known that the catalytic activity of metal or metal oxide particles is also related to their surface area and pore volume.[7,52] The ZnO-NiO composite nanostructures with large BET surface area and pore volume (vide supra) have high catalytic activity, which is beneficial for the thermal decomposition of AP.

EIS with $[Fe(CN)_6]^{3-/4-}$ as indicator has been extensively employed as an effective tool for electrochemical detection of DNA hybridization.[57] In the EIS, the semicircle part corresponds to electron-transfer limited process and its diameter is equal to the electron transfer resistance R_{et} which controls electron transfer kinetics of the redox probe at the electrode interface.[58] The selectivity of the DNA biosensor was investigated by using the

ssDNA probe to hybridize with different DNA sequences. After hybridization of the ssDNA probe, the changes of the Nyquist diagram of 1.0 mmol L^{-1} $[Fe(CN)_6]^{3-/4-}$ are shown in Fig. 9. The curve a is the Nyquist diagram at the probe ssDNA/ZnO/CILE. After the ssDNA probe was hybridized with the cDNA, the change of the Nyquist diagram is shown in curve b. There is a significant increase in the R_{et} value, indicating that hybrids (dsDNA) were formed at the electrode. The increase of the R_{et} value was very little after hybridization of the ssDNA probe with the ncDNA (curve c), suggesting that the hybridization reaction was not accomplished. When the ssDNA probe was hybridized with the single-base mismatched DNA (curve d) or double-base mismatched DNA (curve e), the R_{et} value also increased, which was much smaller than that obtained from the hybridization with the cDNA (curve b). And therefore the single-base mismatched and double-base mismatched DNA could also be sensed via comparing the change of the R_{et} value. The results demonstrated that this DNA biosensor exhibited fine selectivity for the hybridization detection. However, ZnO-NiO composite nanoparticles are not used as the support for probe immobilization since NiO phytotoxicity leads to DNA damage.

The difference between the R_{et} values of 1.0 mmol L^{-1} $[Fe(CN)_6]^{3-/4-}$ at the ssDNA/ZnO/CPE and that at the hybridization modified electrode (dsDNA/ZnO/CILE) was labelled as ΔR_{et}, which was used as the detection signal for quantitative analysis of the PML/RARA fusion gene target sequence. The concentration of the PML/RARA fusion gene target sequence in the hybridization solution was varied from 1.0×10^{-12} to 1.0×10^{-8} mol L^{-1}, and the Nyquist diagrams are shown in Fig. 10. The ΔR_{et} value between before and after hybridization was linear with the logarithm of concentrations of the PML/RARA fusion gene target sequence from 1.0×10^{-12} to 1.0×10^{-8} mol L^{-1}, and a detection limit of 2.2×10^{-13} mol L^{-1} was estimated using 3σ rule (where σ was the relative standard deviation of 11 parallel measurements of the blank solution). The results indicate that the label-free strategy based on

this ZnO/CILE platform exhibited high sensitivity for electrochemical detection of DNA hybridization.

Conclusion

In this work, porous ZnO and ZnO-NiO composite nano/microspheres have been synthesized by a simple precursor method. Further investigations show that the as-obtained ZnO and ZnO-NiO composite nano/microspheres have good abilities to decrease decomposition temperature of AP, which make them useful for application in AP-based composite solid rocket propellants. In addition, EIS measurements demonstrate that the DNA biosensor based on porous ZnO functionalized CILE have a wide detection range with a low detection limit for DNA hybridization. The developed DNA biosensors are expected to have further application in the detection of the PML-RARA fusion gene in real samples in future work.

Acknowledgements

This work was financially supported by the National Natural Science Foundation of China (Grant no. 21331002 and 21205057).

References

1 N. L. Rosi, J. Eckert, M. Eddaoudi, D. T. Vodak, J. Kim, M. O'Keeffe and O. M. Yaghi, *Science*, 2003, **300**, 1127.

2 T. K. Maji, R. Matsuda and S. Kitagawa, *Nat. Mater.*, 2007, **6**, 142.

3 H. Guo, Y. Zhu, S. Wang, S. Su, L. Zhou and H. Zhang, *Chem. Mater.*, 2012, **24**, 444.

4 K. M. L. Taylor-Pashow, J. D. Rocca, Z. G. Xie, S. Tran and W. B. Lin, *J. Am. Chem. Soc.*, 2009, **131**, 14261.

5 D. Zacher, O. Shekhah, C. Wöll and R. A. Fischer, *Chem. Soc. Rev.*, 2009, **38**, 1418.

6 F. Gao, H. Pang, S. P. Xu and Q. Y. Lu, *Chem. Commun.*, 2009, 3571.

7 L. N. Jin, Q. Liu and W.Y. Sun, *CrystEngComm*, 2012, **14**, 7721.

8 S. J. Yang, T. Kim, J. H. Im, Y. S. Kim, K. Lee, H. Jung and C. R. Park, *Chem. Mater.*, 2012, **24**, 464.

9 Z. W. Xu, H. J. Li, W. Li, G. X. Cao, Q. L. Zhang, K. Z. Li, Q. G. Fu and J. Wang, *Chem. Commun*., 2011, **47**, 1166.

10 D. Du, M. H. Wang, Y. H. Qin and Y. H. Lin, *J. Mater. Chem.*, 2010, **20**, 1532.

11 A. McLaren, T. Valdes-Solis, G. Q. Li and S. C. Tsang, *J. Am. Chem. Soc.*, 2009, **131**, 12540.

12 D. J. Gargas, M. E. Toimil-Molares and P. D. Yang, *J. Am. Chem. Soc.*, 2009, **131**, 2125.

13 K. Sun, W. Wei, Y. Ding, Y. Jing, Z. L. Wang and D. L. Wang, *Chem. Commun.*, 2011, **47**, 7776.

14 X. D. Wang, J. Zhou, J. H. Song, J. Liu, N. S. Xu and Z. L. Wang, *Nano Lett.*, 2006, **6**, 2768.

15 Z. L. Wang and J. H. Song, *Science*, 2006, **312**, 242.

16 W. Zhang, X. W. Zheng and K. Jiao, *Sens. Actuat. B*, 2012, **162**, 396.

17 M. Ahmad, C. F. Pan, Z. X. Luo and J. Zhu, *J. Phys. Chem. C*, 2010, **114**, 9308.

18 G. Tang, Y. Wen, A. Pang, D. Zeng, Y. Zhang, S. Tian, B. Shan and C. Xie, *CrystEngComm*, 2014, **16**, 570.

19 J. Yin, F. Gao, C. Wei and Q. Lu, *Sci. Reports*, 2014, **4**, 1.

20 Z. J. Gu, M. P. Paranthaman, J. Xu and Z. W. Pan, *ACS Nano*, 2009, **3**, 273.

21 M. H. Kumar, N. Yantara, S. Dharani, M. Graetzel, S. Mhaisalkar, P. P. Boix and N. Mathews, *Chem. Commun.*, 2013, **49**, 11089.

22 S. Xu, Y. Ding, Y. Wei, H. Fang, Y. Shen, A. K. Sood, D. L. Polla and Z. L. Wang, *J. Am. Chem. Soc.*, 2009, **131**, 6670.

23 P. X. Gao, Y. Ding, W. Mai, W. L. Hughes, C. Lao and Z. L. Wang, *Science*, 2005, **309**, 1700.

24 X. Y. Kong, Y. Ding, R. Yang and Z. L. Wang, *Science*, 2004, **303**, 1348.

25 E. S. Jang, J. H. Won, Y. W. Kim, X. Chen and J. H. Choy, *CrystEngComm*, 2010, **12**, 3467.

26 C. Zhu, B. Lu, Q. Su, E. Xie and W. Lan, *Nanoscale*, 2012, **4**, 3060.

27 H. Q. Yan, R. R. He, J. Pham and P. D. Yang, *Adv. Mater.*, 2003, **15**, 402.

28 G. Q. Zhang, L. Yu, H. E. Hostera and X. W. Lou, *Nanoscale*, 2013, **5**, 877.

29 S. Ding, T. Zhu, J. S. Chen, Z. Wang, C. Yuan and X. W. Lou, *J. Mater. Chem.*, 2011, **21**, 6602.

30 J. Wang, L. M. Wei, L. Y. Zhang, J. Zhang, H. Wei, C. H. Jiang and Y. F. Zhang, *J. Mater. Chem.*, 2012, **22**, 20038.

31 Y. Ren, W. K. Chim, S. Y. Chiam, J. Q. Huang, C. Pi and J. S. Pan, *Adv. Funct. Mater.*, 2010, **20**, 3336.

32 J. Wang, C. Wei, H. Pang, F. Gao, J. Yin, L. Guan and Q. Y. Lu, *Catal. Commun.*, 2011, **12**, 1031.

33 X. Song, L. Gao and S. Mathur, *J. Phys. Chem. C*, 2011, **115**, 21730.

34 X. F. Chu, X. Zhu, Y. Dong, T. Chen, M. Ye and W. Sun, *J. Electroanal. Chem.*, 2012, **676**, 20.

35 N. G. Cho, H. S. Woo, J. H. Lee and I. D. Kim, *Chem. Commun.*, 2011, **47**, 11300.

36 L. Xu, R. Zheng, S. Liu, J.Song, J. Chen, B. Dong and H. W. Song, *Inorg. Chem.*, 2012, **51**, 7733.

37 X. Ma, X. Feng, J. Guo, H. Cao, X. Suo, H. Sun and M. Zheng, *Appl. Catal. B: Environ.*, 2014, **147**, 666.

38 H. Liu, Q. Jiao, Y. Zhao, H. Li, C. Sun, X. Li and H. Wu, *Mater. Lett.*, 2010, **64**, 1698.

39 D. K. Prusty and A. Herrmann, *J. Am. Chem. Soc.*, 2010, **132**, 12197.

40 Y. B. Hahn, R. Ahmadwa and N. Tripathy, *Chem. Commun.*, 2012, **48**, 10369.

41 A. Sassolas, B. D. Leca-Bouvier and L. J. Blum, *Chem. Rev.*, 2008, **108**, 109.

42 A. Kaushik, P. R. Solanki, A. A. Ansari, B. D. Malhotra and S. Ahmad, *Biochem. Eng. J.*, 2009, **46**, 132.

43 S. Zuo, L. Zhang, H. H. Yuan, M. B. Lan, G. A. Lawrance and G. Wei, *Bioelectrochem.*, 2009, **74**, 223.

44 H. Zhu, J. Wang and G. Xu, *Cryst. Growth & Des.*, 2009, **9**, 633.

45 W. Zhang, *Sens. Actuat. B*, 2013, **176**, 386.

46 F. Li, Y. Feng, P. J. Dong and B. Tang, *Biosens. Bioelectron.*, 2010, **25**, 2084.

47 L. B. Wang, X. W. Zheng, W. Zhang, X. Quan, Q. Hu, W. Wu, P. Zong and M. Wu, *RSC Adv.*, 2013, **3**, 9042.

48 J. Wang, S. Li and Y. Zhang, *Electrochim. Acta*, 2010, **55**, 4436.

49 D. Britt, C. Lee, F. J. Uribe-Romo, H. Furukawa and O. M. Yaghi, *Inorg. Chem.* 2010, **49**, 6387.

50 A. R. Millward and O. M. Yaghi, *J. Am. Chem. Soc.*, 2005, **127**, 17998.

51 R. P. Fitzgerald and M. Q. Brewster, *Combust Flame*, 2004, **3**, 313.

52 N. Li, Z. Geng, M. Cao, L. Ren, X. Zhao, B. Liu, Y. Tian and C. W. Hu, *Carbon*, 2013, **54**, 124.

53 Z. Zhou, S. Tian, D. Zeng, G. Tang and C. Xie, *J. Alloy Compd.*, 2012, **513**, 213.

54 N. Li, M. H. Cao, Q. Y. Wu and C. W. Hu, *CrystEngComm*, 2012, **14**, 428.

55 J. Lu, J. Zhu, Z. S. Wang, J. L. Cao and X. F. Zhou, *Ceram. Int.*, 2014, **40**, 1489.

56 B. Varghese, M. Reddy, Y. Zhu, C. Lit, T. C. Hoong, G. V. S. Rao, B. V. R. Chowdari, A. Wee, C. Lim and C. Sow, *Chem. Mater.*, 2008, **20**, 3360.

57 S. Mohan, P. Nigam, S. Kundu and R. Prakash, *Analyst*, 2010, **135**, 2887.

58 A. Kaushik, P. R. Solanki, A. A. Ansari, B. D. Malhotra and S. Ahmad, *Biochem. Eng. J.*, 2009, **46**, 132.

Figure captions:

Scheme 1 Scheme for synthesis of ZnO-NiO composite nanospheres.

Fig. 1 SEM images of (a, b) Zn-CPPs and (c, d) Ni(II)-doped Zn-CPPs nano/microspheres.

Fig. 2 Standard spectrum of ZnO and NiO (a), PXRD patterns of (b) ZnO and (c) ZnO-NiO composite nano/microspheres.

Fig. 3 SEM images of (a) ZnO and (b) ZnO-NiO composite nano/microspheres.

Fig. 4 TEM image (a, b) and HRTEM image (c, d) of ZnO-NiO composite nanospheres.

Fig. 5 EDS mapping of ZnO-NiO composites. SEM images (left) and the corresponding elemental distributions of Ni(II) (middle) and Zn(II) (right).

Fig. 6 DSC curves of (a) pure AP, (b) AP + 2 wt% ZnO and (c) AP + 2 wt% ZnO-NiO composites.

Fig. 7 TGA curves of (a) pure AP, (b) AP + 2 wt% ZnO and (c) AP + 2 wt% ZnO-NiO composites.

Fig. 8 Dependence of $\ln(\beta/T_p^2)$ on $1/(RT_p)$, for AP and mixtures of AP with different additives. Scatter points are experimental data and lines denote the linear fitting results.

Fig. 9 Nyquist diagrams of 1.0 mmol L^{-1} $[Fe(CN)_6]^{3-/4-}$ in 0.1 mol L^{-1} KCl recorded at (a) ssDNA/ZnO/CILE, (b) dsDNA/ZnO/CILE (hybridization with cDNA), (c) the electrode hybridized with ncDNA, (d) the electrode hybridized with single-base mismatched DNA and (e) the electrode hybridized with double-base mismatched DNA.

Fig. 10 Nyquist diagrams of 1.0 mmol L^{-1} $[Fe(CN)_6]^{3-/4-}$ in 0.1 mol L^{-1} KCl recorded at (a) ssDNA/ZnO/CILE and after hybridization reaction with different concentrations of PML/RARA fusion gene target sequence: (b) 1.0×10^{-12}, (c) 1.0×10^{-11}, (d) 1.0×10^{-10}, (e) 1.0×10^{-9} and (f) 1.0×10^{-8} mol L^{-1}.

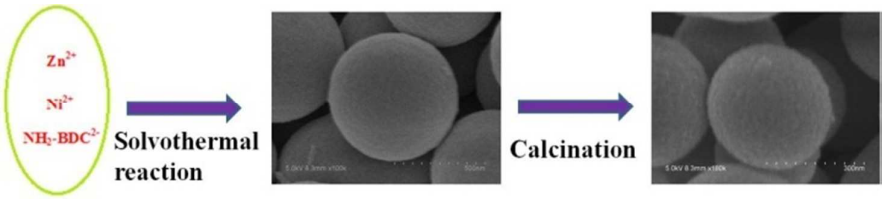

Scheme 1

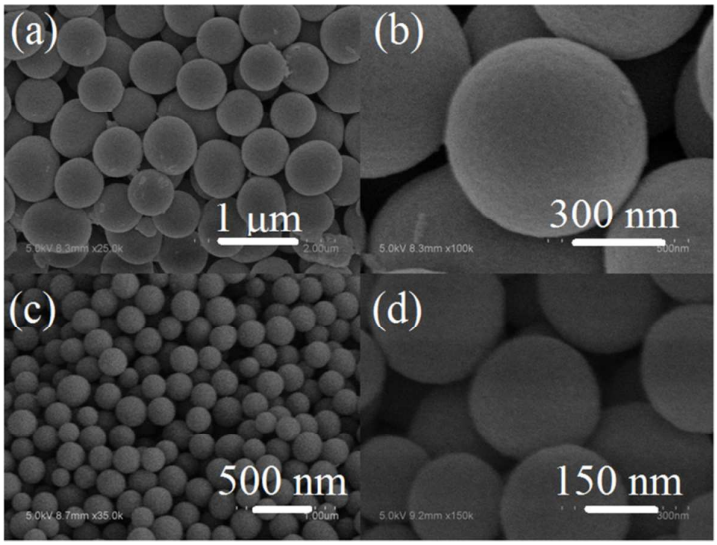

Fig. 1

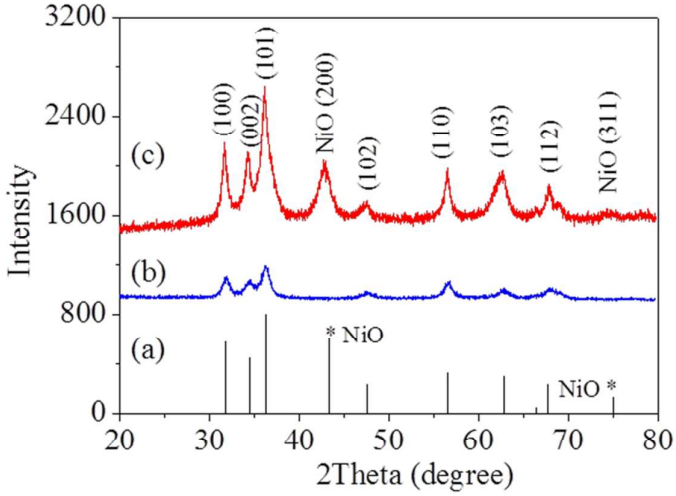

Fig. 2

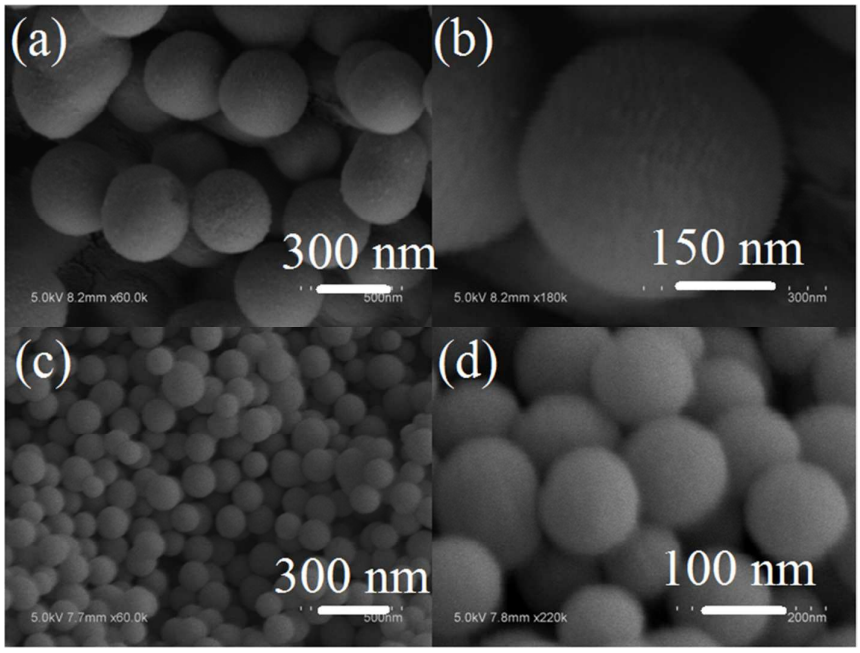

Fig. 3

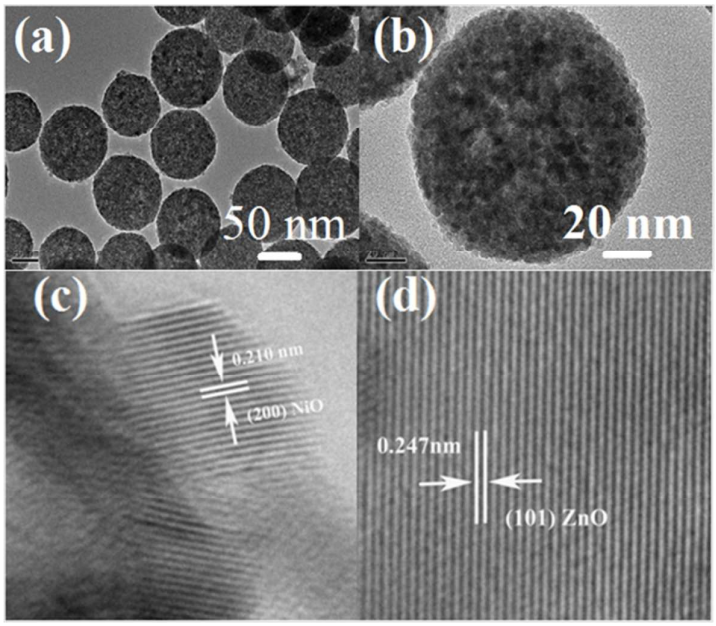

Fig. 4

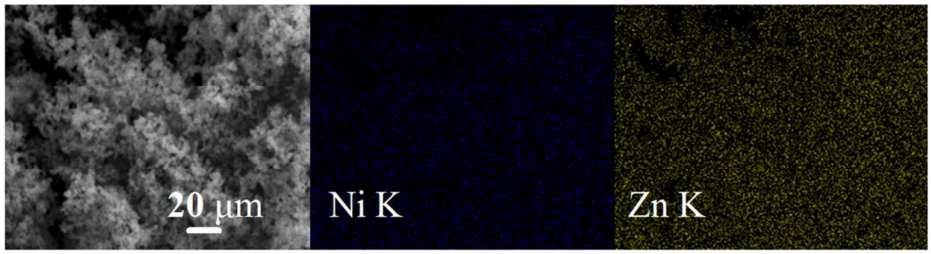

Fig. 5

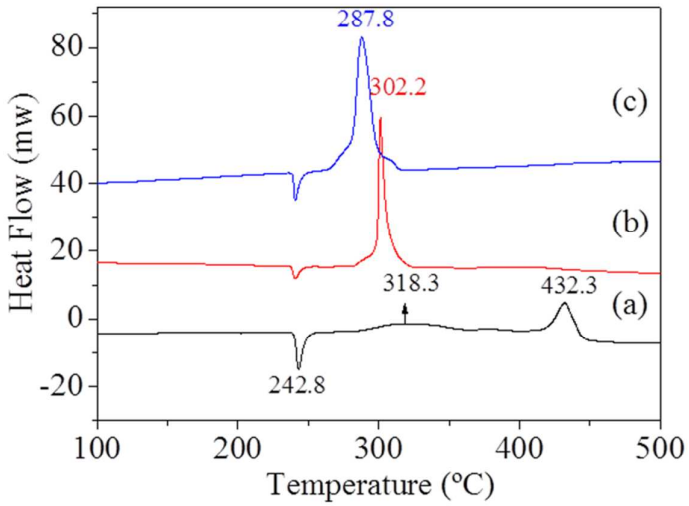

Fig. 6

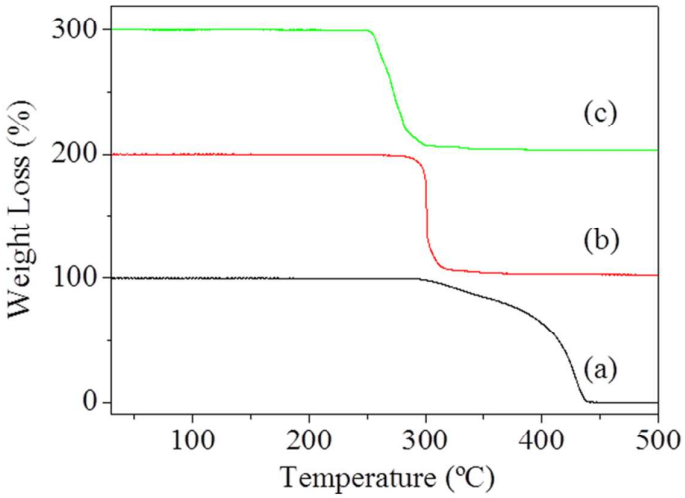

Fig. 7

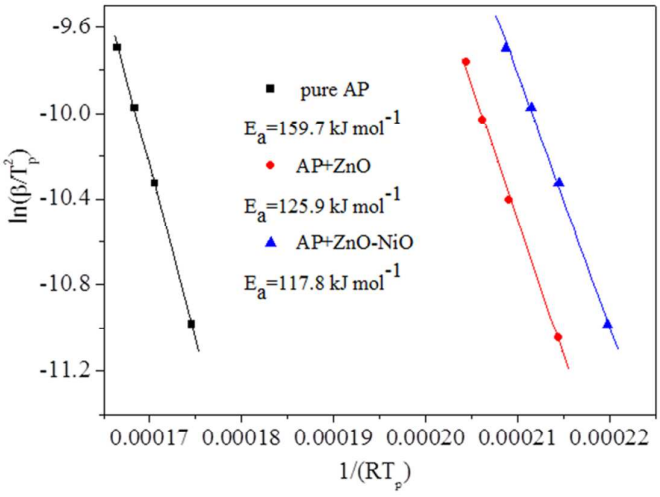

Fig. 8

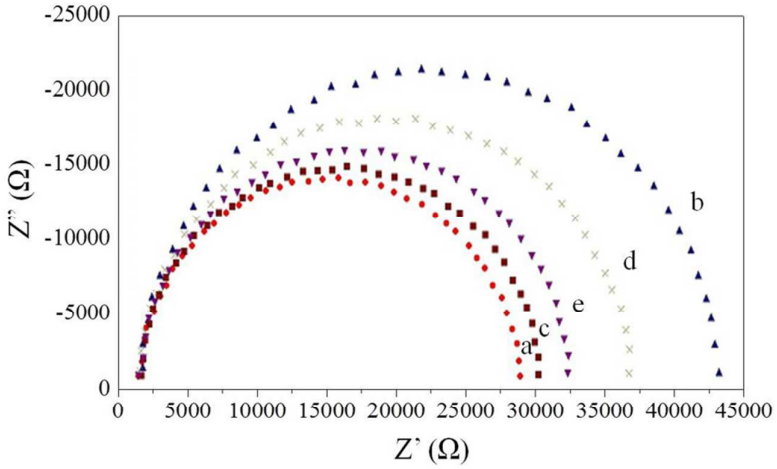

Fig. 9

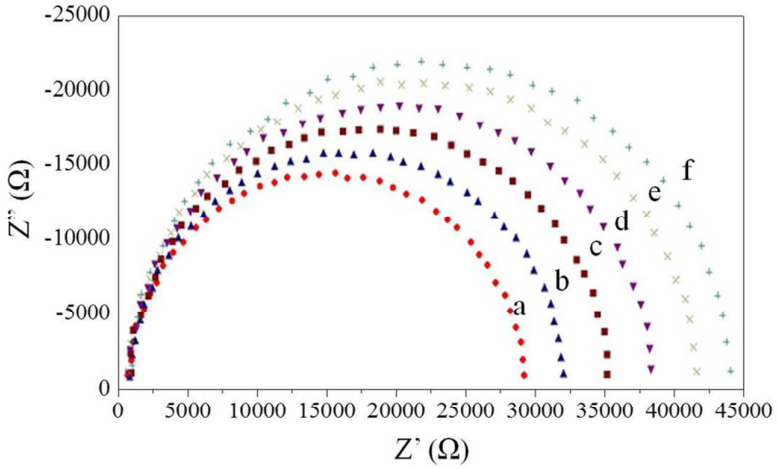

Fig. 10